VII International Conference on Computational Methods for Coupled Problems in Science and Engineering
COUPLED PROBLEMS 2017
M. Papadrakakis, E. Oñate and B. Schrefler (Eds)

COMPUTATIONAL STUDY OF FLOW–INDUCED OSCILLATION OF A SIMPLIFIED SOFT PALATE

M. Ehsan Khalili*, Martin Larsson † and Bernhard Müller *

* Department of Energy and Process Engineering
Norwegian University of Science and Technology (NTNU)
Kolbjørn Hejes vei 2, NO-7491 Trondheim, Norway
e-mail: {mohammadtaghi.khalili, bernhard.muller}@ntnu.no

† Sportradar AS
Ferjemannsveien 10, NO-7014 Trondheim, Norway
e-mail: m.larsson@sportradar.com

Key words: Fluid structure interaction; High order finite difference method; Arbitrary Lagrangian–Eulerian formulation

Abstract. Two-dimensional numerical simulations are employed to study fluid structure interaction of a simplified model of the soft palate in the pharynx for uniform inhalation. We take a next step towards a better biomechanical system by modeling the motion of an inextensible flexible plate. The improved structural model discretized by a low order difference method permits us to simulate the two-dimensional motion of the flexible plate. The inspiratory airflow is described by the Navier–Stokes equations for compressible flow solved by a high order difference method. The explicitly coupled fluid structure interaction model is based on the Arbitrary Lagrangian–Eulerian formulation.

1 Introduction

Fluid structure interaction (FSI) refers to the interaction of a flexible structure with fluid flow where the fluid and structure interact over a shared interface. FSI gives rise to a rich variety of physical phenomena with applications in many fields of engineering and biomechanics. One of the prime examples of FSI in biomechanical systems is the dynamics of the upper airways where the interaction between inspiratory and expiratory airflow with soft tissues may lead to flow-induced oscillations and instabilities. Failure to maintain the patency of the upper airway during sleep characterizes obstructive sleep apnea (OSA), a common and disabling disorder wherein the soft palate obstructs the upper airways for prolonged periods of time during sleep. OSA and snoring are closely related to the flow conditions in the upper airways. Snoring is often considered a minor affliction. But when snoring is heavy, it is often associated with the more crippling condition known as OSA.

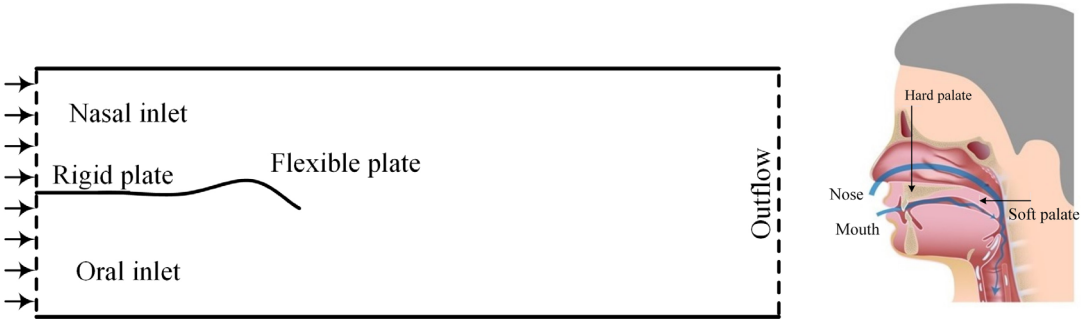

(a) Schematic of the computational model

(b) The anatomy of upper airways.

Figure 1: Computational model and real geometry.

Estimates show that the obstructive sleep apnea syndrome (OSAS) affects 2–4% of the adult population [1] and 10% of snorers are at risk of OSAS [2].

A cantilevered flexible plate immersed in two-dimensional channel flow has previously been shown to capture FSI representative of respiratory airflow and soft-palate dynamics in the upper airway [3, 4, 5, 6]. This is a well-established model wherein a flexible plate representing the soft palate is mounted downstream of a rigid plate representing the hard palate. The rigid plate separates the upper and lower channel flows modeling the flow in the oral and nasal tracts, which interact with the flexible plate motion and then combine into a single channel flow representing the flow in the pharynx, as illustrated in Fig. 1. In these studies, an inviscid flow model was used and viscous effects were implicitly modeled either through the imposition of the Kutta–Joukowski condition [3, 5, 6] or an applied channel resistance [4].

Latterly, researchers have modeled the effects of fluid viscosity explicitly for the laminar regime of Reynolds numbers [7] and investigated constant pressure-drop boundary conditions [8]. In these studies across the low-to-high range of Reynolds numbers, thin plates have been observed to lose their stability at a critical value of flow speed or Reynolds number based on channel height. The destabilization mechanism has been attributed to an irreversible energy transfer from the fluid flow to the plate arising from a phase difference between fluid pressure and plate motion owing to the finite length of the flexible plate [6, 7, 9]. Recently, compressible viscous flow has been employed for this model to characterize the acoustic wave propagation induced by the plate oscillation [10].

In all the studies mentioned above, linear structural mechanics was taken into account by using the one-dimensional Euler–Bernoulli beam equation. Another structural model has been developed by including an inextensibility condition , however, in the interaction with potential flow [11]. Apparently, the soft palate undergoes displacements beyond the linear range, particularly during episodes of obstructed breathing. The soft tissue in the palate is also nearly incompressible and is subjected to fluid friction in a viscous flow field.

Accordingly, the present work accounts for those effects and thereby yields a more faithful biomechanical FSI model. To achieve this, we extend our previous cantilevered plate model [10] to a two-dimensional elastic plate model having an inextensibility condition immersed in compressible viscous flow. This paper presents the development of the improved FSI model and then demonstrates its applicability in simulating flow-induced oscillation of a flexible plate and the characterization of its behaviour in the upper airway.

After outlining the flow and structure models as well as their coupling for FSI, the in-vacuum oscillation of the plate is presented through a verification study of the structural mechanism. Thereafter, the FSI model is used to simulate the flow-induced oscillation of a flexible plate.

2 Model

2.1 Fluid flow

The fluid motion is described by the 2D compressible Navier–Stokes equations in perturbation form. The perturbation formulation is employed to minimize cancellation errors when discretizing the Navier–Stokes equations for compressible low Mach number flow [12, 13, 14]. The conservative form of the 2D compressible Navier–Stokes equations in perturbation formulation can be written as

$$\mathbf{U}'_t + \mathbf{F}^{c'}{}_x + \mathbf{G}^{c'}{}_y = \mathbf{F}^{v'}{}_x + \mathbf{G}^{v'}{}_y \ , \tag{1}$$

where $\mathbf{U}' = \mathbf{U} - \mathbf{U_0}$ is the vector of conservative perturbation variables with $\mathbf{U} = (\rho, \rho u, \rho v, \rho E)^T$ the vector of the conservative variables and $\mathbf{U}_0 = (\rho_0, 0, 0, (\rho E)_0)^T$ the stagnation values. For a complete description of the compressible flow equations, see [10].

2.1.1 Discretization of the compressible Navier–Stokes equations

The high order finite difference method based on summation by parts (SBP) operators [15, 16, 17] is employed for space discretization of the compressible Navier–Stokes equations. We use a globally fourth order SBP operator to discretize the first derivatives and apply them twice to approximate the second derivatives in the viscous terms. The SBP operators correspond to the sixth order central difference operator in the interior, but degrade to third order accuracy near the boundary resulting in fourth order global accuracy [16]. This approach is based on the energy method, which permits us to derive well-posedness for the continuous problem and to guarantee stability for the discrete problem. For the time integration process, the classical fourth order explicit Runge–Kutta method is used. The multi-block structured grid approach is employed to represent the simplified geometry in the upper airways.

Adiabatic no-slip boundary conditions are applied at the walls and the fluid-structure interface. At the inflow, the velocities in the x- and y-directions are imposed using a uniform inlet profile normal to the boundary, $u(x = 0, t) = U_0$ and $v = 0$. In addition,

the inlet temperature is set to $T = T_0 = 310$ K. The outlet pressure is set to atmospheric pressure, i.e., $p' = p - p_0 = p - p_{\text{atm}} = 0$ Pa. The Navier–Stokes characteristic boundary conditions (NSCBC) developed by [18] are employed at the inflow and outflow boundaries to minimize wave reflections. The details of this numerical algorithm and boundary conditions can be found in our previous publication [10].

2.2 The structure model

The plate model is central in order to obtain physical results for simulating the soft palate motion. In the present study, the soft palate is modeled as a two–dimensional, massive, flexible and inextensible plate. This model provides the correlation between the elastic deflection of the plate and the applied force. The flexible plate has its own material density ρ_s, different from the surrounding fluid density ρ_f. The flexibility allows the plate to bend and to react to the force applied by the fluid flow and the flexural force generating a restoring force. Taking into account the inextensibility constraint, the length of the plate remains constant even if an external force is acting on it.

The dynamics of the plate in Lagrangian coordinate s along its undeformed reference configuration can be described by the following equation [19]

$$\rho_s \frac{\partial^2 \mathbf{X}}{\partial t^2} = \frac{\partial}{\partial s}\Big(T\frac{\partial \mathbf{X}}{\partial s}\Big) - \frac{\partial^2}{\partial s^2}\Big(K_B \frac{\partial^2 \mathbf{X}}{\partial s^2}\Big) + \rho_s \mathbf{g} + \mathbf{F}, \tag{2}$$

where s is the arclength, $\mathbf{X} = (x(s,t), y(s,t))^T$ denotes the material position of the plate, T is the tension along the Lagrangian coordinate s, K_B is the flexural rigidity, $\mathbf{g}$ the gravitational acceleration, and $\mathbf{F}$ is the force applied on the plate by the surrounding fluid. Furthermore, ρ_s is the actual line density of the plate defined as the line density difference between the thin plate and the surrounding fluid $\rho_s = \rho - \rho_f A$, where ρ is density of the plate, ρ_f the density of the fluid and A is the cross sectional area of the plate.

The inextensibility constraint of the plate [20, 19], i.e. the local stretching of the plate satisfies $\frac{d}{dt}|\frac{\partial \mathbf{X}}{\partial s}| = 0$, can be expressed as

$$\frac{\partial \mathbf{X}}{\partial s} \cdot \frac{\partial \mathbf{X}}{\partial s} = 1. \tag{3}$$

Following the previous studies [20, 19], the tension T in this model is determined by a Poisson equation derived by inserting the constraint of inextensibility Eq. (3) into the dot product of $\frac{\partial \mathbf{X}}{\partial s}$ and the $s-$derivative of the plate dynamical equation Eq. (2)

$$\frac{\partial \mathbf{X}}{\partial s} \cdot \frac{\partial^2}{\partial s^2}\Big(T\frac{\partial \mathbf{X}}{\partial s}\Big) = \frac{\rho_s}{2}\frac{\partial^2}{\partial t^2}\Big(\frac{\partial \mathbf{X}}{\partial s} \cdot \frac{\partial \mathbf{X}}{\partial s}\Big) - \rho_s \frac{\partial^2 \mathbf{X}}{\partial t \partial s} \cdot \frac{\partial^2 \mathbf{X}}{\partial t \partial s} - \frac{\partial \mathbf{X}}{\partial s} \cdot \frac{\partial}{\partial s}\Big(\mathbf{F}_B + \mathbf{F}\Big) \tag{4}$$

where $\mathbf{F}_B$ is the bending force which by using the Euler–Bernoulli assumption for a thin flexible plate is expressed as

$$\mathbf{F}_B = -\frac{\partial^2}{\partial s^2}\left(K_B \frac{\partial^2 \mathbf{X}}{\partial s^2}\right) \tag{5}$$

The non-dimensional parameters are chosen with respect to the stagnation density ρ_0, stagnation speed of sound c_0 and the length of the flexible plate L, in the same way as for the fluid solver.

The boundary conditions are specified at the free end ($s = L$) and at the fixed end at ($s = 0$) of the plate. The free end boundary condition at the trailing edge is imposed by assuming that the tension, bending moment and shear force are zero

$$T(L,t) = 0, \quad \left.\frac{\partial^2 \mathbf{X}}{\partial s^2}\right|_{s=L} = 0, \quad \left.\frac{\partial^3 \mathbf{X}}{\partial s^3}\right|_{s=L} = 0 \tag{6}$$

The support mechanism at the leading edge is taken into account as

$$\mathbf{X}|_{s=0} = \mathbf{X}_0, \quad \left.\frac{\partial^2 \mathbf{X}}{\partial s^2}\right|_{s=0} = 0 \tag{7}$$

2.2.1 Discretization of the structure model

The discretisation of the governing equation of the plate motion (2) along s is performed on a staggered grid following [19]. The plate is discretized with a finite number of Lagrangian points $\mathbf{X}_i$. The plate tension is defined at the interfaces of the grid cells, and other variables are defined at the primary grid points in the centers of the grid cells, as shown in Fig. 2

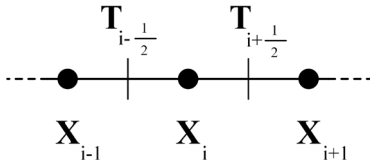

Figure 2: Schematic diagram of staggered grid discretisation on the plate along its Lagrangian coordinate.

Then, the numerical procedure for the non-dimensionalised form of Eqs. (2) and (3) is as follows

$$\mathbf{X}^* = 2\mathbf{X}_i^n - \mathbf{X}_i^{n-1} \tag{8}$$

$$\mathbf{F}_B^* = -D_{ss}(K_B \; D_{ss}\mathbf{X}^*)_i^n \tag{9}$$

$$(D_s\mathbf{X}^*)_{i+\frac{1}{2}} \cdot \Big(D_s(D_s(T^{n+\frac{1}{2}}_{i+\frac{1}{2}} D_s\mathbf{X}^*))\Big) = \rho_s \frac{1 - 2(D_s\mathbf{X} \cdot D_s\mathbf{X})^n_{i+\frac{1}{2}} + (D_s\mathbf{X} \cdot D_s\mathbf{X})^{n-1}_{i+\frac{1}{2}}}{2\Delta t^2} - \rho_s(D_s\mathbf{V} \cdot D_s\mathbf{V})^n_{i+\frac{1}{2}} - (D_s\mathbf{X}^*)^n_{i+\frac{1}{2}} \cdot \Big(D_s(\mathbf{F}^*_B + \mathbf{F}^n)\Big)_{i+\frac{1}{2}} \tag{10}$$

$$\rho_s \frac{\mathbf{X}^{n+1}_i - \mathbf{X}^*_i}{\Delta t^2} = \Big(D_s(T^{n+\frac{1}{2}} D_s\mathbf{X}^{n+1})\Big)_i + (\mathbf{F}_B)^{n+1} + \mathcal{G}\frac{\mathbf{g}}{|g|} + \mathbf{F}^n_i \tag{11}$$

where D_s and D_{ss} are the second order accurate difference operators for the first and second derivatives along s, respectively, and $\mathbf{X}^*$ is the predicted position of the plate. Employing $\mathbf{X}^*$ to calculate the tension helps to reduce the error. The tension is computed at the intermediate step, i.e. $t^{n+\frac{1}{2}}$ and is employed to update the position of the plate, i.e. $\mathbf{X}^{n+1}$. The velocity of the plate is defined as $\mathbf{V}^n_i = (\mathbf{X}^n_i - \mathbf{X}^{n-1}_i)/\Delta t$. $\mathbf{F}^n$ denotes the force exerted by the fluid flow on the structure and is obtained explicitly using the fluid solver at time level n. $\mathcal{G}$ is defined as the non-dimensional gravity $\mathcal{G} = gL/c_0^2$. Equations (10) and (11) constitute diagonally dominant tri- and pentadiagonal linear systems, which are solved by LU decomposition without pivoting, i.e. by the Thomas algorithm and a similar algorithm, respectively. The condition for diagonal dominance of the matrix in Eq. (11) is $K_B \frac{\Delta t^2}{\Delta s^4} \leqslant \frac{1}{4}$.

2.3 Fluid structure interaction

To handle the fluid flow in Eulerian description using moving fluid grids and the plate structure in a Lagrangian formulation using stationary structure grids, the Arbitrary Lagrangian–Eulerian (ALE) formulation is appropriately employed. Considering the velocity of the fluid grids $\dot{x}$ and $\dot{y}$ in the time-dependent coordinate transformation of the fluid flow domain, the grid point velocities are subtracted from the fluid velocity to define the contravariant velocity components $U = \xi_x(u-\dot{x})+\xi_y(v-\dot{y})$ and $V = \eta_x(u-\dot{x})+\eta_y(v-\dot{y})$ which yield simple expressions for the transformed inviscid flux vectors $\hat{\mathbf{F}}^c$ and $\hat{\mathbf{G}}^c$ [21]. The mesh update is implemented by remeshing the whole fluid domain in each time step using the positions and velocities of the flexible structure at the boundary and a linear interpolation for interior points in the fluid domain.

Solving fluid flow on a moving mesh, the numerical scheme should satisfy the Geometric Conservation Law (GCL) for mathematical consistency [22], which leads to the 2D Navier-Stokes equations in ALE formulation [23] being expressed as

$$\mathbf{U}'_\tau = \tfrac{1}{J^{-1}}(-\hat{\mathbf{F}}'_\xi - \hat{\mathbf{G}}'_\eta - (J^{-1})_\tau \mathbf{U}'). \tag{12}$$

An explicit, two-way method where forces and deformations are exchanged between the flow and the deformable structure in each time-step is employed to handle the coupling between the fluid and the structure. The fluid and structure interact with each other by applying equal displacement and velocity at the interface, satisfying the no-slip and adiabatic wall boundary conditions. The force exerted by the fluid flow on the plate at

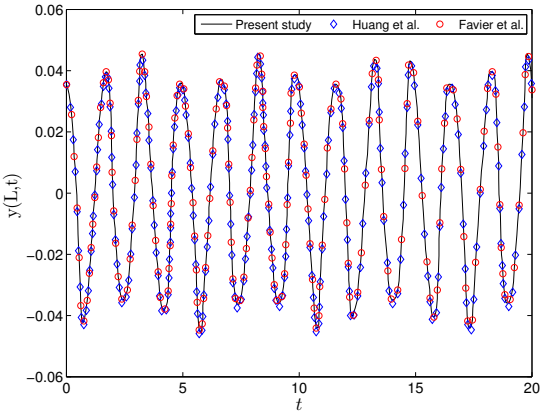

Figure 3: Time history of the y-coordinate position of the trailing edge of the plate subjected to only gravity, without bending force $K_B = 0$. The solid line shows the present model, circles present the results of the study performed by Huang et al. [19] and diamonds represent the results of the study done by Favier et al. [24].

time level n in equations (10) and (11) is given by $\mathbf{F}^n = -(p_U^n - p_L^n)\mathbf{n}$, where p_U and p_L are the pressures on the upper side and lower side of the plate, respectively, and $\mathbf{n}$ is the outer unit vector normal to the plate.

3 Results and discussion

3.1 Verification of structure solver in vacuum

The accuracy of the numerical model of the plate has been first tested and verified by simulating the oscillation and bending of the plate subjected to the gravity force in the absence of surrounding fluid, i.e. a pendulum with gravity acting in the $x-$direction. The plate was initially deformed by using the following initial configuration

$$\mathbf{X}(s,0) = \mathbf{X}_0 + s(\cos\theta, \sin\theta), \quad s \in [0, L], \tag{13}$$

where L is the length of the plate, θ is an angle and $\mathbf{X}_0 = (0,0)$. This particular configuration within the small angle approximation is considered in previous studies [19, 24]. Following them, the test is first performed by setting the initial angle of the plate to $\theta = 0.01\pi$ with a flexural stiffness $K_B = 0$ and non-dimensional gravity equivalent to $\gamma = 10$. The length of the plate is $L = 1$, and it is discretized by $N = 101$ grid points along the Lagrangian coordinate s. The time variation of the y coordinate of the trailing edge is monitored and shown in Fig. 3.

A second verification test is performed for a larger initial deflection angle $\theta = 0.1\pi$ and by including the non-dimensional bending force with $K_B = 0.01$. Fig. 4 illustrates the y-displacement of the trailing edge and the time variation of the plate deformation.

The results obtained in Figures 3 and 4(a) are in good agreement in comparison with

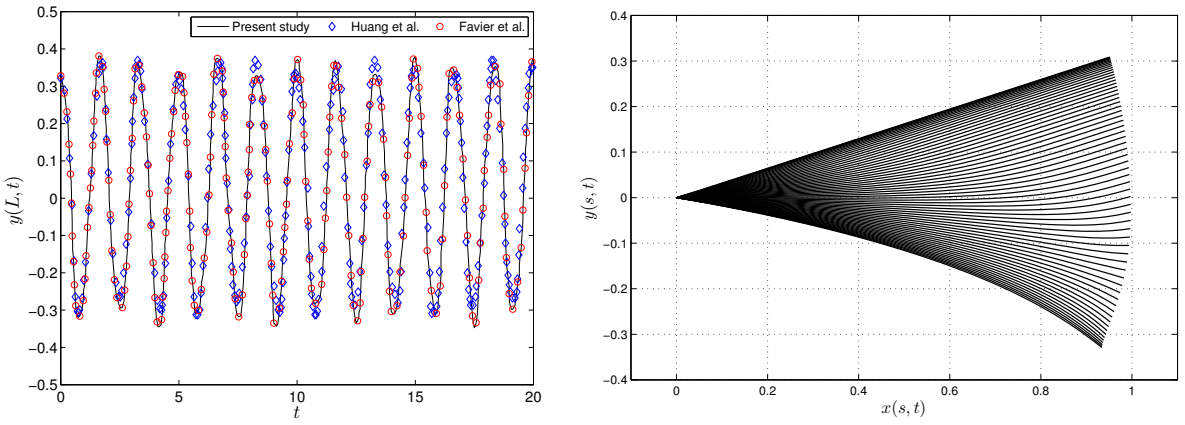

(a) (b)

Figure 4: (a) Time history of the y-coordinate position of the trailing edge of the plate subjected to only gravity $\gamma = 10$, with bending force $K_B = 0.01$. The solid line shows the present model, circles present the results of the study performed by Huang et al. [19] and diamonds represent the results of the study done by Favier et al. [24], (b) The sequence of superposition of the plate from up to down between time $0 - 0.8$.

the available numerical results [19, 24].

3.2 Numercal results of FSI

Having established the credibility of the structural model, we now couple the structure and fluid models to investigate their interaction. The computational domain is a rectangular channel with $0 \leq x \leq 9L$ and $0 \leq y \leq 4L$ where L is the length of the flexible plate. The flexible plate modeling the soft palate is attached to a rigid plate with length L representing the hard palate. The origin of the rigid plate is located in the middle of the height of the channel. Therefore, the leading edge of the flexible plate is placed at $(L, 2L)$. Overall, the computational domain is discretized by 581×281 grid points in longitudinal and transversal directions, respectively. The Reynolds number $\mathrm{Re} = \frac{\rho U L}{\mu} = 378$ and the Mach number $\mathrm{Ma} = \frac{U}{c_0} = 0.1$ are used based on the inlet velocity, density, viscosity, speed of sound and the plate length. The nondimensional line density $\frac{\rho_s}{\rho_0 L}$ is 1, and the nondimensional flexural rigidity $\frac{K_B}{\rho_0 c_0^2 L^3} = 0.0001$ is used. The plate is discretized by $N = 81$ grid points and $\frac{\Delta t c_0}{L} = 0.001$ is chosen. The initial configuration of the flexible plate is a straight line like in the previous section with $\theta = -0.04\pi$. The flexible plate has been fixed to its initial displacement until an approximately steady state flow solution is reached at $\frac{t c_0}{L} = 60$. Then, the flexible plate is released from its initial position and allowed to interact with the flow.

Fig. 5 represents the y-displacement of the trailing edge and the time variation of the plate deformation. The amplitude of the oscillation is decreasing, and the frequency is

about $\frac{fL}{c_0} = 0.6$.

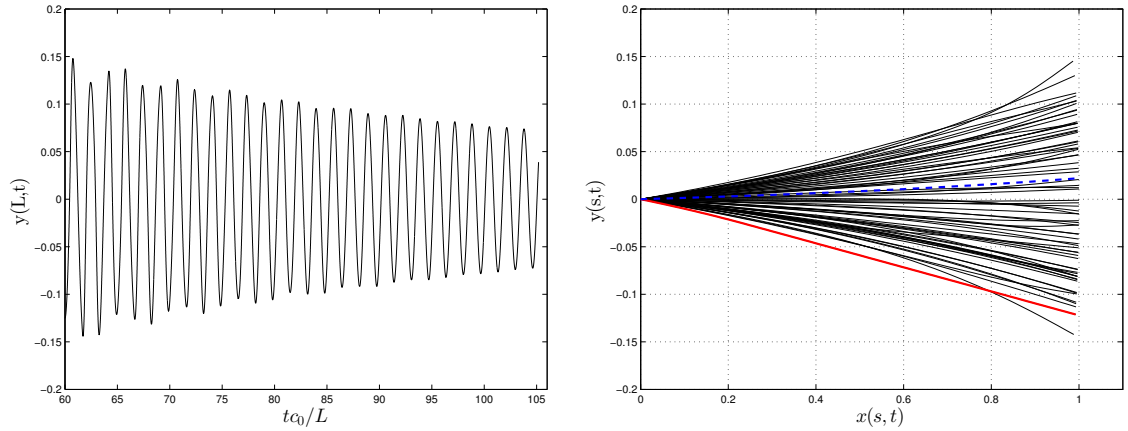

(a) (b)

Figure 5: (a) Time history of the y-coordinate position of the trailing edge of the plate in FSI. (b) Sequence of flexible plate deformation from $tc_0/L = 60$ to $tc_0/L = 105$, the initial and final deformation are marked by the red solid line and the blue dashed line, respectively.

Fig. 6 shows the instantaneous spanwise vorticity contours in the left column and the corresponding pressure field on the right at five time instants. The plate is released to oscillate at nondimensional time $tc_0/L = 60$. The plate oscillation produces a strong acoustic wave near the trailing edge of the plate. The wave hits the top and bottom wall of the channel and the reflected waves propagate into the domain, hitting waves newly produced by oscillating plate and waves reflected the at the inlet. These reflected waves interact and produce a complex interference pattern which leads a very noisy pressure field. The complexity of the reflections and vicinity of the inlet boundary imposing uniform flow to the trailing edge lead to a build-up of vortices near the inlet. Behind the trailing edge of the oscillating plate, a complex vorticity pattern is observed.

4 Conclusions

In the present study, we have implemented a two-dimensional structure model to interact with compressible viscous flow in order to simulate the fluid structure interaction for a simplified model of the soft palate in the pharynx. The soft palate is modeled as a deformable inextensible plate. The FSI algorithm is based on the Arbitrary Lagrangian–Eulerian formulation with an explicit, two-way coupling strategy. The 2D compressible Navier–Stokes equations are computed by highly stable high order summation by parts (SBP) difference operators. The explicit Runge–Kutta method is applied for time integration. The structure model is solved by an implicit second order difference method to determine the flexible plate motion. The accuracy of the structural solver has been as-

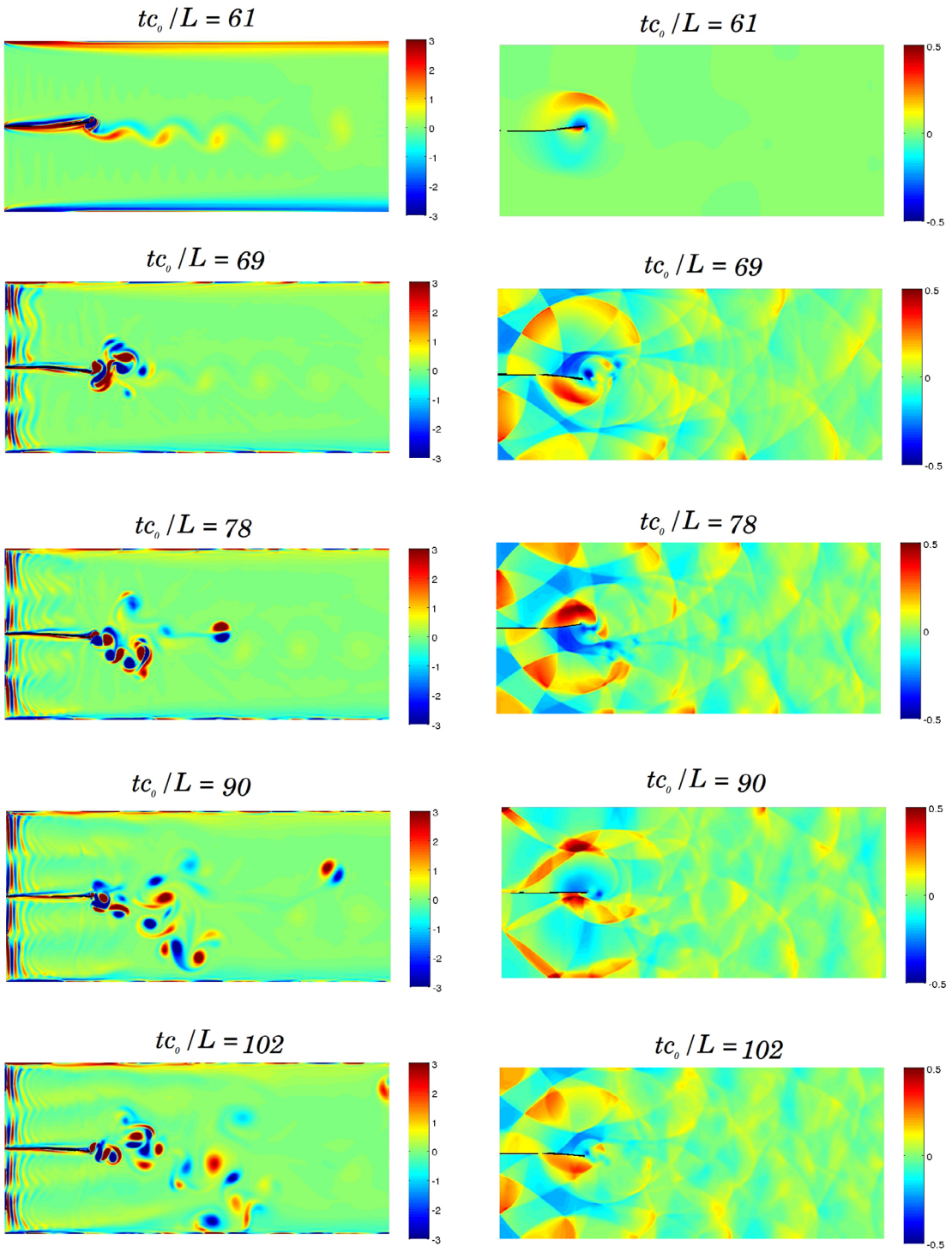

Figure 6: The left column shows the time sequence of vorticity contour plots, $\frac{\omega_z L}{c_0}$, and the right column presents the corresponding acoustic pressure contour plots, $\frac{p'}{\rho_0 c_0}$, at Re = 378 and Ma = 0.1.

sessed through comparisons with previous numerical results. The flow-induced oscillation of the plate is simulated for low Reynolds and Mach numbers. Strong acoustic waves are produced by the oscillating plate. Complex pressure and vorticity patterns are observed.

REFERENCES

[1] T. Young, M. Palta, J. Dempsey, J. Skatrud, S. Weber, and S. Badr, "The occurrence of sleep-disordered breathing among middle-aged adults," *New England Journal of Medicine*, vol. 328, no. 17, pp. 1230–1235, 1993.

[2] C. D. Bertram, "Flow-induced oscillation of collapsed tubes and airway structures," *Respiratory Physiology & Neurobiology*, vol. 163, no. 1, pp. 256–265, 2008.

[3] L. Huang, "Flutter of cantilevered plates in axial flow," *Journal of Fluids and Structures*, vol. 9, no. 2, pp. 127–147, 1995.

[4] Y. Auregan and C. Depollier, "Snoring: Linear stability analysis and in-vitro experiments," *Journal of Sound and Vibration*, vol. 188, no. 1, pp. 39–53, 1995.

[5] C. Guo and M. Païdoussis, "Stability of rectangular plates with free side-edges in two-dimensional inviscid channel flow," *Journal of Applied Mechanics*, vol. 67, no. 1, pp. 171–176, 2000.

[6] R. Howell, A. Lucey, P. Carpenter, and M. Pitman, "Interaction between a cantilevered-free flexible plate and ideal flow," *Journal of Fluids and Structures*, vol. 25, no. 3, pp. 544–566, 2009.

[7] T. Balint and A. Lucey, "Instability of a cantilevered flexible plate in viscous channel flow," *Journal of Fluids and Structures*, vol. 20, no. 7, pp. 893–912, 2005.

[8] G. Tetlow and A. D. Lucey, "Motions of a cantilevered flexible plate in viscous channel flow driven by a constant pressure drop," *Communications in Numerical Methods in Engineering*, vol. 25, no. 5, pp. 463–482, 2009.

[9] L. Tang, M. P. Païdoussis, and J. Jiang, "Cantilevered flexible plates in axial flow: energy transfer and the concept of flutter-mill," *Journal of Sound and Vibration*, vol. 326, no. 1, pp. 263–276, 2009.

[10] M. Khalili, M. Larsson, and B. Müller, "Interaction between a simplified soft palate and compressible viscous flow," *Journal of Fluids and Structures*, vol. 67, pp. 85–105, 2016.

[11] L. Tang and M. P. Païdoussis, "On the instability and the post-critical behaviour of two-dimensional cantilevered flexible plates in axial flow," *Journal of Sound and Vibration*, vol. 305, no. 1, pp. 97–115, 2007.

[12] J. Sesterhenn, B. Müller, and H. Thomann, "On the cancellation problem in calculating compressible low Mach number flows," *Journal of Computational Physics*, vol. 151, no. 2, pp. 597–615, 1999.

[13] B. Müller, "High order numerical simulation of aeolian tones," *Computers & Fluids*, vol. 37, no. 4, pp. 450–462, 2008.

[14] M. Larsson and B. Müller, "Numerical simulation of confined pulsating jets in human phonation," *Computers & Fluids*, vol. 38, no. 7, pp. 1375–1383, 2009.

[15] B. Strand, "Summation by parts for finite difference approximations for d/dx," *Journal of Computational Physics*, vol. 110, no. 1, pp. 47–67, 1994.

[16] B. Gustafsson, *High order difference methods for time dependent PDE*. Berlin: Springer, 2008.

[17] B. Gustafsson, H.-O. Kreiss, and J. Oliger, *Time dependent problems and difference methods*. New York: John Wiley & Sons, 1995.

[18] T. J. Poinsot and S. Lele, "Boundary conditions for direct simulations of compressible viscous flows," *Journal of Computational Physics*, vol. 101, no. 1, pp. 104–129, 1992.

[19] W.-X. Huang, S. J. Shin, and H. J. Sung, "Simulation of flexible filaments in a uniform flow by the immersed boundary method," *Journal of Computational Physics*, vol. 226, no. 2, pp. 2206–2228, 2007.

[20] A.-K. Tornberg and M. J. Shelley, "Simulating the dynamics and interactions of flexible fibers in Stokes flows," *Journal of Computational Physics*, vol. 196, no. 1, pp. 8–40, 2004.

[21] T. H. Pulliam and J. L. Steger, "Implicit finite-difference simulations of three-dimensional compressible flow," *AIAA Journal*, vol. 18, no. 2, pp. 159–167, 1980.

[22] M. R. Visbal and D. V. Gaitonde, "On the use of higher-order finite-difference schemes on curvilinear and deforming meshes," *Journal of Computational Physics*, vol. 181, no. 1, pp. 155–185, 2002.

[23] R. Peyret, H. Viviand, and J. Smolderen, "Computation of viscous compressible flows based on the Navier-Stokes equations," *NASA STI/Recon Technical Report N*, vol. 76, p. 11380, 1975.

[24] J. Favier, A. Revell, and A. Pinelli, "A lattice Boltzmann–immersed boundary method to simulate the fluid interaction with moving and slender flexible objects," *Journal of Computational Physics*, vol. 261, pp. 145–161, 2014.